Computational Materials Science 184 (2020) 109864

Contents lists available at ScienceDirect

Computational Materials Science

journal homepage: www.elsevier.com/locate/commatsci

Atomistic simulations of the face-centered-cubic-to-hexagonal-close-packed phase transformation in the equiatomic CoCrFeMnNi high entropy alloy under high compression

Kang-Tien Hsieh[a], You-Yi Lin[a], Chi-Hung Lu[a], Jer-Ren Yang[a], Peter K. Liaw[b], Chin-Lung Kuo[a,*]

[a] Department of Materials Science and Engineering, National Taiwan University, Taipei 10617, Taiwan
[b] Department of Materials Science and Engineering, The University of Tennessee, Knoxville, TN 37996, USA

ARTICLE INFO

Keywords:
CoCrFeMnNi high-entropy alloy
High compression
Molecular dynamics simulations
FCC-HCP phase transformation

ABSTRACT

We performed the modified-embedded-atom-method (MEAM) based molecular dynamics (MD) simulations to investigate the plastic deformation and phase transformation behaviors in the CoCrFeMnNi HEA under high compression at room temperature. Our MD simulations revealed that the stress-induced phase transformations in the CoCrFeMnNi HEA are strongly crystal orientation-dependent. The [0 0 1] uniaxial compression can induce the significant face-centered-cubic (fcc) -to-hexagonal-close-packed (hcp) phase transformation via successive emissions of partial dislocations from the extended stacking faults, twin boundaries and hcp-lamellas created during the early stage of deformation. As for the [1 1 0] and [1 1 1] uniaxial compressions, however, the transformed hcp atoms can simply form the intrinsic/extrinsic stacking faults. Although the [0 0 1] uniaxial compression produced a much lower dislocation density than the other two systems, it induced much more constituents transformed into the hcp atoms at the end of phase transformation. Our results clearly indicated that the deformation twin boundaries and extended hcp-lamellas play a critical role in facilitating the stress-induced fcc-to-hcp phase transformation in the CoCrFeMnNi HEA. Furthermore, it was found that the phase transformation in the CoCrFeMnNi HEA can be effectively facilitated by a large deviatoric compressive stress while it may tend to be significantly retarded by a hydrostatic compression. Our results also showed that the plastic deformation behaviors in Ni under high compression are very similar to those occurred in the CoCrFeMnNi HEA though nearly all the hcp atoms can simply constitute the intrinsic/extrinsic stacking faults without the formation of any bulk hcp phase in the fcc lattice. The main discrepancy in the phase transformation behaviors between the Ni and CoCrFeMnNi HEA can be largely attributed to the much lower stacking fault energy of the CoCrFeMnNi HEA than other fcc metals.

1. Introduction

High-entropy alloys (HEAs) have recently attracted considerable research interest primarily owing to their many exceptional and fascinating properties, such as the remarkably high ultimate tensile strength, uniform elongation [1–4], and significantly improved radiation and corrosion resistance, in comparison to other conventional alloys [5–13]. HEAs generally refer to a single phase solid-solution alloy with five or more principal elements in an equiatomic or near-equiatomic chemical composition [14,15]. The term “high-entropy” denotes the high configurational entropy inside a material system, which can inhibit the formation of intermetallic compounds and stabilize the single solid-solution phase in a simple crystal structure, such as face-centered-cubic (fcc), body-centered-cubic (bcc), and hexagonal-close-packed (hcp) structures [14,15]. Among the various HEAs reported in the literatures, the equiatomic fcc CoCrFeMnNi alloy is one of the most notable prototype HEAs, possessing relatively high mechanical strength, fracture toughness, and superior ductility particularly at the cryogenic temperatures as compared with other conventional alloys [16–18]. The unique combination of these exceptional properties is mainly attributed to the strong solid-solution strengthening effect, the increased dislocation-dislocation interaction, and the ease of nano-twin formation in the fcc CoCrFeMnNi HEA upon plastic deformation. Many experimental studies revealed that the CoCrFeMnNi HEA can retain the stable fcc single-phase structure from the cryogenic temperature range up to the melting point without any polymorphic phase transformation occurred [2,17,18]. This high structural stability is generally believed to be due to the extremely sluggish atomic diffusion in the CoCrFeMnNi HEA by

* Corresponding author.
E-mail address: chinlung@ntu.edu.tw (C.-L. Kuo).

https://doi.org/10.1016/j.commatsci.2020.109864
Received 15 March 2020; Received in revised form 3 June 2020; Accepted 5 June 2020
Available online 18 June 2020
0927-0256/

its chemical complexity and local packing disorder [10]. Nevertheless, recent first-principles free-energy calculations suggested that the hcp phase of the CoCrFeMnNi HEA is more thermodynamically favorable than its fcc counterpart at room temperature, resulting in a relatively lower stacking fault energy than other fcc metals [19–21].

Very recently, Tracy et al. reported a high-pressure synthesis of the hcp phase of the CoCrFeMnNi HEA, in which a sluggish martensitic transformation from the fcc to hcp phases was observed to start at ~14.0 GPa, and ~60% of the ingrown hcp phase was retained as being quenched to the ambient condition [22]. Almost simultaneously, Zhang et al.'s *in-situ* synchrotron XRD experiment also revealed a polymorphic transformation from fcc to hcp phases in the CoCrFeMnNi HEA under hydrostatic compression, in which the phase transition started at ~22 GPa and almost completed at ~41 GPa [23]. Their results showed that the hcp phase can be retained as the pressure was fully released and almost completely transformed back to the fcc phase when it was heated up to 723 K. Moreover, using a similar experimental technique, Huang et al. evidenced the same irreversible phase transformation but the onset pressure of phase transition appeared to be much lower (~7 GPa) [24]. On the other hand, Zhang et al. also reported a pressure-induced fcc-to-hcp phase transformation in the quaternary CoCrFeNi HEA with a transition pressure starting at 13.5 GPa and a weight ratio of ~36% hcp phase at 39 GPa [25]. However, Ahmad et al.'s *in-situ* high-pressure XRD measurements showed that the fcc CoCrFeMnNi HEA remained stable without any amorphization or phase transformation occurred as the pressure was raised up to 49 GPa [26]. Yu et al. prepared the CoCrFeMnNi HEA by mechanical alloying and high-pressure sintering, showing that the alloy still retained the fcc structure without the appearance of any hcp phase as the pressure increased up to 31 GPa [27]. The large discrepancy in the onset pressure of phase transition from 7 to 49 GPa was mainly ascribed to different levels of the nonhydrostaticity induced by different pressure mediums as suggested by Zhang et al. [28]. Their results showed that a larger deviatoric stress induced by the pressure media can effectively reduce the onset pressure, thereby promoting the polymorphic fcc-to-hcp phase transformation in the CoCrFeMnNi HEA. These studies indeed shed light on a new route to fabricate the new hcp or fcc-hcp dual-phase HEAs with tunable material properties using the high-pressure processing method. Nevertheless, current understanding regarding the detailed mechanisms of this polymorphic phase transformation is still very limited. Although the hcp structure can be readily obtained by introducing stacking faults into the fcc lattice, the atomistic mechanisms associated with the dislocation properties and twinning events in the CoCrFeMnNi HEA upon plastic deformation can be far more complex than expected.

Atomistic simulation is a powerful tool to investigate the structural, kinetic, thermodynamic and mechanical properties of metals and alloys, providing a mechanistic understanding of the underlying mechanisms of complex materials phenomena at the atomic-scale. First-principles density functional theory calculations are presently the most reliable and widely used approach to predict the fundamental properties of materials, which have become a necessity in the modern materials research to complement the experimental analyses. However, due to the limitation of the time and length scale, it remains rather difficult to study the plastic deformation behaviors and the associated defect/dislocation interactions in metallic materials using first-principles modeling techniques, where the time scale and system size can be up to a few nanoseconds and 10^6 atoms. An alternative approach is to apply the semi-empirical interatomic-potential-based techniques, which employ a set of parameterized functions aiming at representing the potential-energy hypersurface of a material system. Hence, the accuracy of an interatomic potential model relies on not only its mathematical functions but also the availability of a reliable parameter set that can accurately describe all the interactions between the constituent elements in the alloy systems considered. From this perspective, the modified embedded atom method (MEAM) [29] is an ideal interatomic-potential model for the CoCrFeMnNi HEA since it can describe a wide range of elements within different structures using the same mathematical formalism. The MEAM potential was later extended by Lee and Baskes [30–33] to partially include the second-nearest neighbor interactions (i.e., the so-called 2NN MEAM) towards improving some critical drawbacks of its original formalism. Recently, the unary, binary, and ternary potential parameters of the 2NN MEAM model for the CoCrFeMnNi HEA have been developed by Lee's group based on the experimental data of some fundamental materials properties [34–40]. This success showed great promise in conducting large-scale atomistic simulations to explore the underlying mechanisms of complex materials phenomena in this five-component alloy system.

In the present study, we performed the second nearest-neighbor modified-embedded-atom-method based molecular dynamics simulations to investigate the plastic deformations and fcc-to-hcp phase transformations in the equiatomic CoCrFeMnNi HEA under high compression at room temperature. On the basis of Choi et al.'s work [34,35], we refined the binary and ternary potential parameters to make the calculated mechanical properties in better agreement with those derived from first-principles calculations. Our MD simulations revealed that the stacking faults, twin boundaries and extended hcp-lamellas created during the early stage of deformation can play a critical role in facilitating the stress-induced fcc-to-hcp phase transformation in the CoCrFeMnNi HEA. It was shown that this polymorphic transformation can be effectively facilitated by a large deviatoric compressive stress, while it may tend to be significantly retarded by a hydrostatic compression. Our simulation results also demonstrated that the plastic deformation behaviors in Ni under high compression were very similar to those in the CoCrFeMnNi HEA though there was no bulk hcp phase formed in Ni upon deformation. The main discrepancy in the phase transformation behaviors between the CoCrFeMnNi HEA and Ni can be largely attributed to the much lower stacking fault energy of the CoCrFeMnNi HEA than other fcc metals.

2. Computational details

In this study, we investigated the atomistic mechanisms of the plastic deformation and the fcc-to-hcp phase transformation in the equiatomic CoCrFeMnNi HEA under high compression using molecular dynamic simulations as implemented in the Large-scale Atomic/Molecular Massively Parallel Simulator (LAMMPS) [41]. The interatomic interactions between atoms in the CoCrFeMnNi HEA were described using the second nearest-neighbor modified-embedded-atom-method (2NN MEAM) potentials [30]. In the framework of the 2NN MEAM, the potential energy of a material system is given by

$$E = \sum_i \left[F(\bar{\rho}_i) + 1/2 \sum_{j \neq i} S_{ij} \varphi(R_{ij}) \right] \tag{1}$$

where the first term is the embedding function for atom i embedded in the background electron density $\bar{\rho}_i$, while the second term is the conventional pair-interaction potential between atoms i and j. In the 2NN MEAM, the embedding function is given as follows:

$$F(\bar{\rho}_i) = AE_c(\bar{\rho}_i/\bar{\rho}^0)\ln(\bar{\rho}_i/\bar{\rho}^0) \tag{2}$$

Here A is an adjustable parameter, E_c is the sublimation energy (or cohesive energy), and $\bar{\rho}^0$ is the background electron density for a reference structure. The pair interaction potential $\varphi(R_{ij})$ is multiplied by a many-body screening function S_{ij}, which denotes the level of screening on atoms i and j by other neighboring atoms and is determined by two parameters, C_{min} and C_{max}, that define the range of screening. Although the embedding function has an explicit functional formalism in the 2NN MEAM, there is no specific mathematic function for the pair interaction$\varphi(R_{ij})$, which is generally derived from the universal equation of state proposed by Rose for the total energy of a reference structure [42].

$$E^u(R) = -E_c(1 + a^* + da^{*3})e^{-a^*} \quad (3)$$

$$a^* = \sqrt{\frac{9B\Omega}{E_c}}\left(\frac{R}{r_e} - 1\right) \quad (4)$$

where $E^u(R)$ is the universal function for an isotropic expansion or contraction in the reference structure, E_c is the cohesive energy, R is the nearest-neighbor distance, r_e is the equilibrium nearest-neighbor distance, B is bulk modulus, and Ω is the equilibrium atomic volume of the reference structure. The parameter d is an adjustable variable used to refine the repulsive and attractive regions in the universal equation of state. In the 2NN MEAM, the energy per atom in a reference structure is expressed as follows:

$$E^u(R) = F[\bar{\rho}^0(R)] + (Z_1/2)\varphi(R) + (Z_2S/2)\varphi(aR) \quad (5)$$

Here Z_1 is the number of the first nearest neighbors, Z_2 is the number of the second nearest neighbors, and a is the ratio between the second and first nearest neighbor distance in the reference structure. Since $E^u(R)$ and $F[\bar{\rho}^0(R)]$ are readily obtained from the reference structure, the pair-interaction potential can be directly calculated using Eq. (5). A more detailed description of the mathematical formalisms and the fundamental principles of the 2NN MEAM potentials can be referred to the previous work developed by Lee et al. [30,31].

To describe the atomic interactions in the CoCrFeMnNi HEA, it requires a complete potential parameter set for the unary, binary and ternary interactions among all the constituent elements considered in this alloy system. The parameters of the 2NN MEAM potentials for pure elements, Co, Fe, Mn, and Ni, were obtained directly from the literatures [30,31,34–37]. For the Cr-Cr interactions, we slightly modified the parameters to make the prediction of the bcc/fcc energy difference in better agreement with the first-principles calculations since the cohesive energy of fcc Cr calculated using Choi et al.'s potential parameters is nearly identical to that of bcc Cr. As for the binary systems, we developed the new MEAM cross potential parameters for 10 individual binary pairs, including the Co-Cr, Co-Fe, Co-Mn, Co-Ni, Fe-Cr, Fe-Mn, Fe-Ni, Mn-Ni, Mn-Cr, and Ni-Cr interactions. The lattice constants, elastic moduli and formation energies of each binary alloy in the $L1_2$ (A_3B/AB_3), B1 and B2 (AB) structures were calculated using first-principles calculations, which were then used to determine the parameters, E_c, r_e, B, and d, in the universal equation of state and the screening parameters, C_{min} and C_{max}, for all the binary pairs considered. Furthermore, thirty more parameters for C_{min} and C_{max} are required to describe the ternary interactions in a quinary alloy system, which were determined using a similar approach based on the average concept as suggested by Choi et al. without numerical fitting [34,35]. The complete 2NN MEAM potential parameter sets and the reference structures used for modeling the CoCrFeMnNi HEA were summarized in the supplementary information (SI) with a LAMMPS input file format provided. First-principles calculations performed herein for the development of the 2NN MEAM potential parameters were on the basis of density functional theory (DFT) within the generalized gradient approximation [Perdew-Burke-Ernzerhof (PBE)] as implemented in the Vienna Ab initio Simulation Package (VASP) [43–45]. A detailed description of the calculation conditions used in the present work is provided in the supplementary information for reference.

In this study, the mechanical responses of the fcc CoCrFeMnNi HEA under high compression were investigated by applying uniaxial compressive strains to various supercells along different crystal orientations using isothermal MD simulations at 300 K. For uniaxial compression on the fcc CoCrFeMnNi HEA, we employed three different supercells ($40_{x,[100]} \times 40_{y,[010]} \times 40_{z,[001]}$, $20_{x,[1\bar{1}1]} \times 12_{y,[1\bar{1}\bar{2}]} \times 90_{z,[110]}$, and $60_{z,[110]} \times 12_{y,[1\bar{1}\bar{2}]} \times 30_{x,[1\bar{1}1]}$), each containing 259,200 atoms, to simulate the compressive loadings along the [0 0 1], [1 1 0], and [1 $\bar{1}$ 1] directions, respectively, in which periodic boundary conditions were imposed in all three directions. During the MD simulations, these three supercells were uniaxially compressed at a strain rate of $1.0 \times 10^8\ s^{-1}$, while the unstrained directions were fully relaxed to keep the systems at a minimum stress level. Moreover, the effects of the strain rate on the simulation results have been examined using a strain rate of one-order-of magnitude smaller, showing that the atomistic mechanisms identified in the present work were not affected by the strain rate used. During the MD simulations, the integration of the equation of motion was performed using the Verlet algorithm with an integration time step of 2 fs, and the Nosé-Hoover thermostat was applied to control the temperature of the simulation systems. Furthermore, a radial cutoff distance of 4.0 Å was employed for all static calculations and MD simulations performed herein.

The equilibrium structure model of the CoCrFeMnNi HEA in a single fcc phase was constructed using an in-hose code to generate the special quasi-random structure (SQS), which was obtained by optimizing the Warren-Cowley short-range order (SRO) parameters [46,47] for all possible nearest-neighbor pairs around each constituent element. The procedure and analysis of the HEA models generated were briefly outlined in SI for reference. As for the structural characterization, the coordination number of each atom was calculated to identify the point defects, and lines of atoms with coordination defects generally indicate the presence of dislocations. Furthermore, the common neighbor analysis (CNA) was used to identify whether the atoms are in the locally perfect fcc or hcp lattice arrangements [48], and the open visualization tool, Ovito, was used to assist in the analysis of the plastic deformation and phase transformation processes in the MD simulations [49]. Herein, atoms not in the perfect fcc or hcp local environments were considered as atoms located in the dislocation cores. In an fcc lattice, an intrinsic stacking fault is formed by two adjacent planes of atoms in a locally perfect hcp lattice arrangement, while an extrinsic stacking fault is constituted by two planes of atoms in the perfect hcp local environment separated by a plane of atoms in the locally perfect fcc lattice arrangement. In addition, a single plane of atoms in the locally perfect hcp environment is used to indicate the presence of a twin boundary in a fcc lattice.

3. Results and discussion

The 2NN MEAM potential parameters employed in this work have been examined through a series of validations, including the structural properties of the CoCrFeMnNi and CoCrFeNi HEA in fcc/hcp phases, the relative stability between their fcc and hcp structures, as well as the elastic moduli and stacking fault energies of the CoCrFeMnNi/CoCrFeNi HEA, etc. Our calculations showed that the fundamental properties of the CoCrFeMnNi/CoCrFeNi HEA calculated using the 2NN MEAM potential are in good agreement with those derived from first-principles calculations and available experimental data in the literatures. In particular, the 2NN MEAM potential also predicted the negative stacking fault energies for the equiatomic CoCrFeMnNi, CoCrFeNi, and CoCrNi alloys at 0 K, respectively, which are in accord well with those predicted by the recent first-principles calculations [19–21,50]. On the other hand, the structural properties and energetics of the CoCrFeMnNi/CoCrFeNi HEA predicted by our 2NN MEAM potential parameters are in good consistency with those calculated using the ones developed by Choi et al. [34,35]. Nevertheless, our predictions for their mechanical properties are in better agreement with those obtained from first-principles calculations and the recent experimental data reported. For instance, our predictions for Young's moduli of the fcc CoCrFeMnNi HEA along the [0 0 1], [1 1 0] and [1 1 1] directions (E_{001} = 144 GPa, E_{110} = 265 GPa, and E_{111} = 296 GPa) are in excellent agreement with Huang et al.'s recent experimental measurements (E_{001} = 135 GPa, E_{110} = 225 GPa, and E_{111} = 300 GPa) [51]. Accordingly, these calculations confirmed that the 2NN MEAM potential parameters employed in this work can be reliably used to describe and explore the fundamental properties of the CoCrFeMnNi HEA. These calculated results and comparative validations were summarized in Table S1-S5 in SI, respectively, for reference.

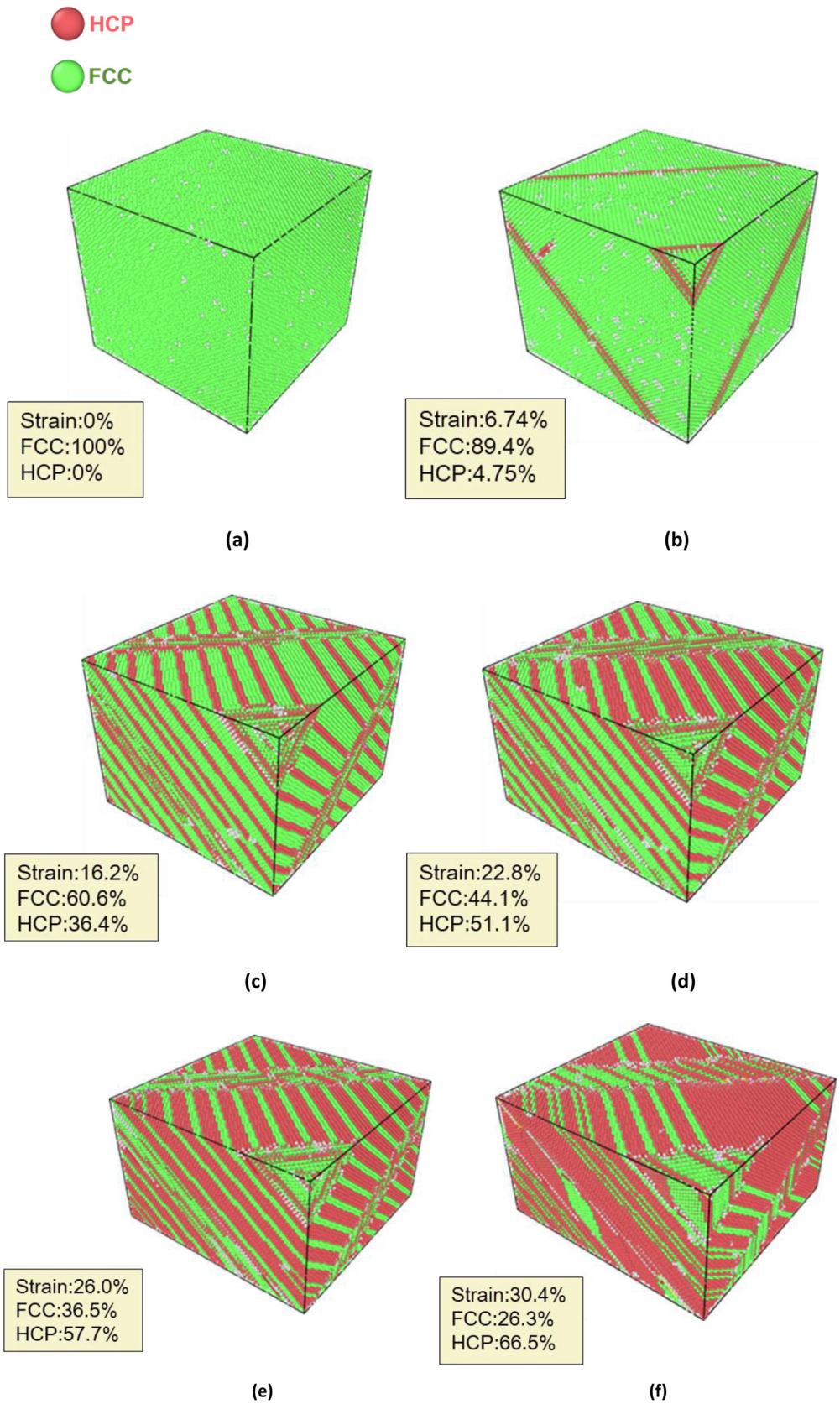

Fig. 1. The structural evolution of the fcc CoCrFeMnNi HEA upon compressive loading along the [0 0 1] direction at various stages of strain levels. The green and brown colors indicate the atoms in the perfect fcc and hcp lattice arrangements, respectively, while the white colored atoms represent the dislocation cores or the highly distorted atoms. (For interpretation of the references to colour in this figure legend, the reader is referred to the web version of this article.)

3.1. Uniaxial compression along the [0 0 1] direction

The mechanical responses of the fcc CoCrFeMnNi HEA upon uniaxial compressions were simulated over the range of strain levels from 0 to 35% to explore the fundamental mechanisms of plastic deformation and fcc-to-hcp phase transformation processes. Fig. 1 presents the snapshots of the structural evolution of the fcc CoCrFeMnNi HEA upon compressive loading along the [0 0 1] direction at various stages of strain levels. Our MD simulations revealed that the structural relaxation in the fcc CoCrFeMnNi HEA under the [0 0 1] uniaxial compression primarily proceeded with the nucleation and glide of 1/6 ⟨1 1 2⟩ –type Shockley partial dislocation loops, leading to the formation of the extended stacking faults in the fcc lattice, which were identified as atoms arranged in a locally perfect hcp environment. The homogeneous nucleation of dislocation loops first occurred as the strain level was increased up to 6.5% with a compressive stress of 9.5 GPa. Once the Shockley partial dislocation loop was formed, it can quickly glide away from the nucleation site to form stacking disorder in the fcc lattice, and the stacking fault density appeared to increase linearly with the strain level during the plastic deformation process. These extended stacking faults may gradually grow into a bulk hcp phase due to the constant nucleation and successive glide of Shockley partial dislocation loops. As the strain level was raised above 30.0%, the whole system has nearly reached an equilibrium state and ended up with 66.5% of the constituent elements transformed into the hcp atoms in the fcc matrix.

Fig. 2 presents an atomistic mechanism of the structure transition during the early stage of the plastic deformation process in the fcc CoCrFeMnNi HEA. Our MD simulations revealed that nano-twins can form at a relatively low strain level (6.5–7.0%) above the yield strain due to the successive glide of Shockley partial dislocation loops on the adjacent {1 1 1} atomic planes along the ⟨1 1 2⟩ directions [also see Fig. 1(b)]. This result was primarily attributed to the low stacking fault energy of the CoCrFeMnNi HEA, which has been experimentally observed at low temperature during the plastic deformation process [1–3]. As illustrated in Fig. 2, the glide of the first Shockley partial dislocation loop created an intrinsic stacking fault in the fcc lattice, which was followed by the subsequent glide of the second and third Shockley partials on the neighboring (1 1 1) planes, resulting in the formation of an extrinsic stacking fault and a three-layer deformation twinned region, respectively. This three-layer twin is separated by two twin boundaries, which can be identified by a single plane of atoms arranged in a locally perfect hcp lattice. Furthermore, besides the homogeneous nucleation of partial dislocation loops, our MD simulations revealed that plenty of Shockley partial dislocations can be heterogeneously nucleated at the twin boundaries and the extended stacking faults created during the early stage of deformation, which effectively facilitated the fcc-to-hcp phase transformation process in the CoCrFeMnNi HEA under the [0 0 1] uniaxial compression.

Fig. 3(a)–(d) illustrates the heterogeneous nucleation of a Shockley partial dislocation pair on one side of an extended intrinsic stacking fault, one of which was emitted into the bulk region creating another new intrinsic stacking fault, while the other one was trapped at the phase boundary between the stacking fault and fcc lattice. In the meanwhile, another pair of Shockley partial dislocations were nucleated and gliding on the other side, which gradually transformed the extended intrinsic stacking fault into an extrinsic one. Subsequently, the originally trapped partial dislocation dissociated into a stair-rod dislocation and a new Shockley partial gliding along the interface between the stacking fault and fcc lattice, which then converted the extrinsic stacking fault into a three-layer deformation twin as illustrated in Fig. 3(e) and (f). It can also be found that another Shockley partial dislocation was emitted from the extended intrinsic stacking fault, which then interacted with the oncoming partial dislocations to form an hcp embryo in the fcc lattice. Furthermore, as presented in Fig. 3(f), a Shockley partial dislocation pair was originally nucleated at a site neighboring to the twin boundary attributed to the considerably high local compressive stress, which then rapidly propagated into the bulk region forming a new intrinsic stacking fault. On the other hand, the

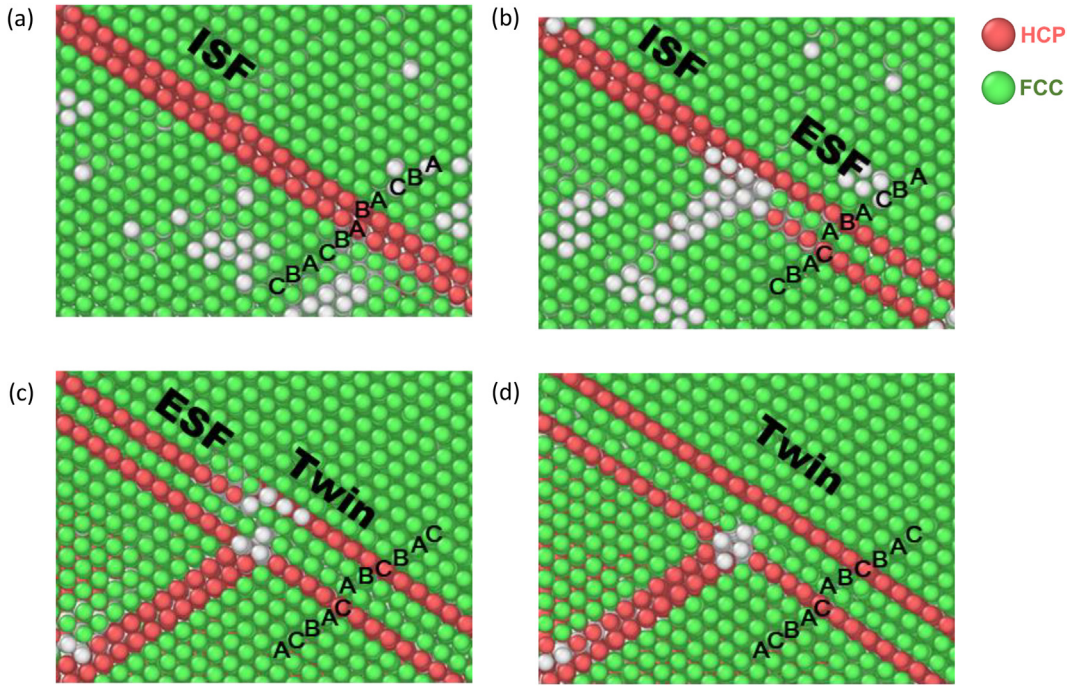

Fig. 2. The atomistic mechanism of the structure transition during the early stage of the plastic deformation at the strain level between 6.5% and 7.0% in the fcc CoCrFeMnNi HEA, in which the glide of the first Shockley partial dislocation loop created an intrinsic stacking fault in (a), followed by the subsequent glide of the second and third Shockley partials on the neighboring (1 1 1) planes resulting in the formation of an extrinsic stacking fault in (b), and then a three-layer deformation twinned region in (c)-(d), respectively. The green and brown colors indicate the atoms in the perfect fcc and hcp lattice arrangements, respectively, while the white colored atoms represent the under-coordinated atoms such as the dislocation cores or the highly distorted atoms which may also be identified as the under-coordinated atoms by Ovito. (For interpretation of the references to colour in this figure legend, the reader is referred to the web version of this article.)

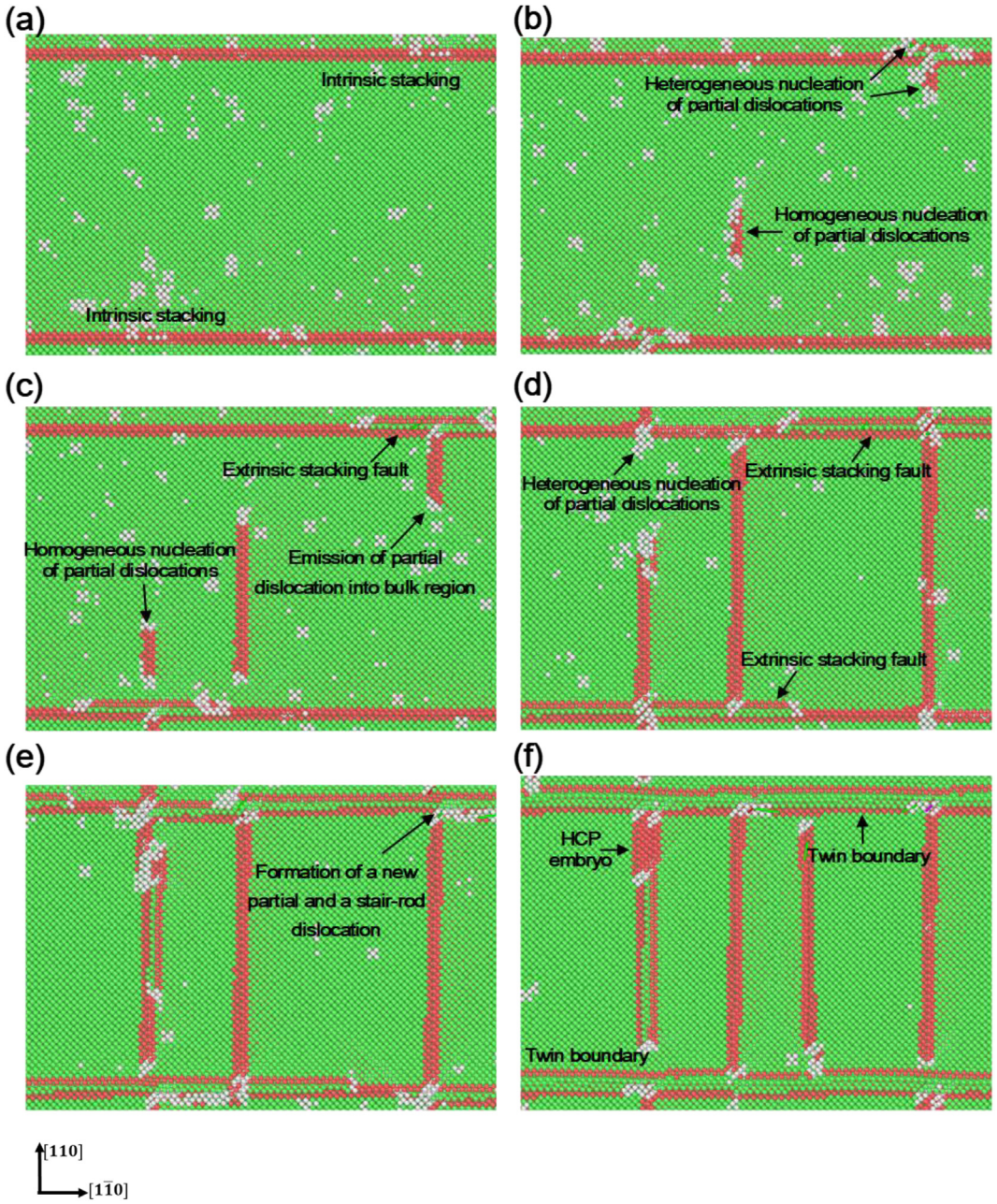

Fig. 3. Heterogeneous nucleation of partial dislocations on the extended intrinsic stacking faults can be created during the early stage of deformation. These Shockley partials can be either emitted into the bulk region creating another new intrinsic stacking fault, or glide on the extended intrinsic stacking faults followed by their transformation into the extrinsic stacking faults and the twin boundaries. The green and brown colors indicate the fcc and hcp atoms, respectively, while the white colored atoms are the dislocation cores or the highly distorted atoms. In Fig. 2(a)-(c), there were many highly distorted atoms in the bulk fcc region or near the stacking faults, some of which were then nucleated to form partial dislocations and stacking faults during the deformation processes. Accordingly, the local stresses in the bulk fcc region would be substantially relieved and the associated number of highly distorted atoms would also be significantly reduced as shown in Fig. 2(d)-(f). (For interpretation of the references to colour in this figure legend, the reader is referred to the web version of this article.)

interactions of an oncoming Shockley partial dislocation with the extended intrinsic/extrinsic stacking faults and the twin boundaries were also frequently observed in the [0 0 1] uniaxial compression system during the plastic deformation processes [see Fig. 3(c)–(f)].

The supplementary Fig. S1 displays the interaction of a homogeneously nucleated intrinsic stacking fault with an existing twin boundary under sufficiently high compressive loading, where a dislocation reaction occurred, resulting in the creation of two new dislocations at the twin boundary. This dislocation reaction was $\frac{1}{6}[\bar{1}21] \rightarrow \frac{1}{6}[01\bar{1}] + \frac{1}{6}[\bar{1}12]$, where the $\frac{1}{6}[\bar{1}21]$ leading partial of an extended dislocation dissociated into a stair-rod dislocation with a Burgers vector of $\frac{1}{6}[01\bar{1}]$ and a $\frac{1}{6}[\bar{1}12]$ Shockley partial that was free to move on the twin boundary. The stair-rod dislocation was later removed when the $\frac{1}{6}[1\bar{2}\,\bar{1}]$ trailing partial arrived at the twin boundary, yielding the formation of a new $\frac{1}{6}[1\bar{1}\bar{2}]$ Shockley partial dislocation on the twinning plane. Both of these two newly created partial dislocations can glide on the twin boundary in the opposite direction that caused the unzipping of one layer of hcp atoms resulting in the growth of the nano-twin region, which was quite similar to what has been observed in other fcc metals [52–54]. On the other hand, the heterogeneous nucleation and growth of an hcp lamella parallel to the twin boundary was also observed in our MD simulations during the plastic deformation

processes. The supplementary Fig. S2 displays the impingement of a Shockley partial dislocation on a twin boundary under sufficiently high compressive loading, where the glide of the $\frac{1}{6}[\bar{1}21]$ leading partial was hindered by the twin boundary, which in turn facilitated the nucleation of a new Shockley partial with a stair-rod dislocation near the twinning plane. This newly created $\frac{1}{6}[\bar{1}12]$ Shockley partial dislocation was then gliding on an atomic plane neighboring to the twin boundary (i.e., one atomic plane in between was skipped), which subsequently transformed the original twin boundary into a three-layer hcp structure. This newly created hcp lamella may further grow into a thick hcp structure via successive traps of the leading partials of the subsequent incoming extended dislocations, followed by the nucleation and glide of new Shockley partials on a slip plane neighboring to the fcc/hcp phase boundary. Nevertheless, it was also found that the impingement of a partial dislocation on the fcc/hcp phase boundary may also lead to the transformation of one layer of the hcp atoms returning back to the fcc structure, thereby inhibiting the continued growth of the hcp lamella during the plastic deformation processes.

Our MD simulations also revealed that a considerable number of Shockley partial dislocations can be heterogeneously nucleated at the fcc/hcp-lamella interface under sufficiently high compressive strain. Similar to those found at the intrinsic/extrinsic stacking faults and the twin boundaries, one Shockley partial dislocation was emitted from the fcc/hcp-lamella interface into the bulk region forming an extended stacking fault, while the other one was either trapped at the phase boundary or readily dissociated into a stair-rod dislocation and a new Shockley partial gliding in parallel with the fcc/hcp-lamella interface. As the strain level further increased, the intrinsic stacking faults emitted from the fcc/hcp-lamella interface (or the twin boundary) may gradually transform into the four-layer hcp films via the successive glide of the new Shockley partial dislocations on their neighboring (1 1 1) atomic planes [see Fig. 4(a)-(e)]. These four-layer hcp films can further grow into a thicker hcp structure via the continued emissions of Shockley partial dislocations from the twin boundaries and the fcc/hcp-lamella interfaces, which were eventually transformed into a bulk hcp region in the fcc matrix as illustrated in Fig. 4(f). Although the interactions of the twin boundary and the hcp lamella with an incoming Shockley partial dislocation can also lead to the growth of hcp layers along the phase boundaries, they were not observed to grow into a bulk hcp phase due to the constant nucleation of the new partial dislocation loops on these phase boundaries under high compressive loadings. As shown in Fig. 4(c)-(e), there were numerous dislocations reactions occurring near the fcc/hcp-lamella interfaces due to the successive emissions of Shockley partial dislocations from these phase boundaries and the impingements by the incoming extended dislocations, which may locally transform the hcp layers back to the fcc structure. Furthermore, it was also observed that the partial dislocation loops can be homogeneously nucleated inside the hcp-lamella attributed to the relatively high local compressive stresses, thereby leading to the recovery of few layers of the fcc atoms within the hcp structure.

As the strain level kept further increased, the hcp lamella created along the original twin boundary was gradually transformed back to the fcc structure accompanied with the formation of the new twin boundaries and fcc/hcp interfaces. As shown in Fig. 4(f), Shockley partial dislocations were nucleated and emitted sequentially from these newly created twin boundaries and fcc/hcp interfaces to form extended intrinsic stacking faults and new hcp phases in other fcc regions [also see Fig. 1(e)-(f)]. These twin boundaries and fcc/hcp interfaces would eventually turn into the grain boundaries between different hcp structures upon the end of phase transformation. Accordingly, successive emissions of Shockley partial dislocations from the extended stacking faults, twin boundaries, and the fcc/hcp-lamella interfaces created

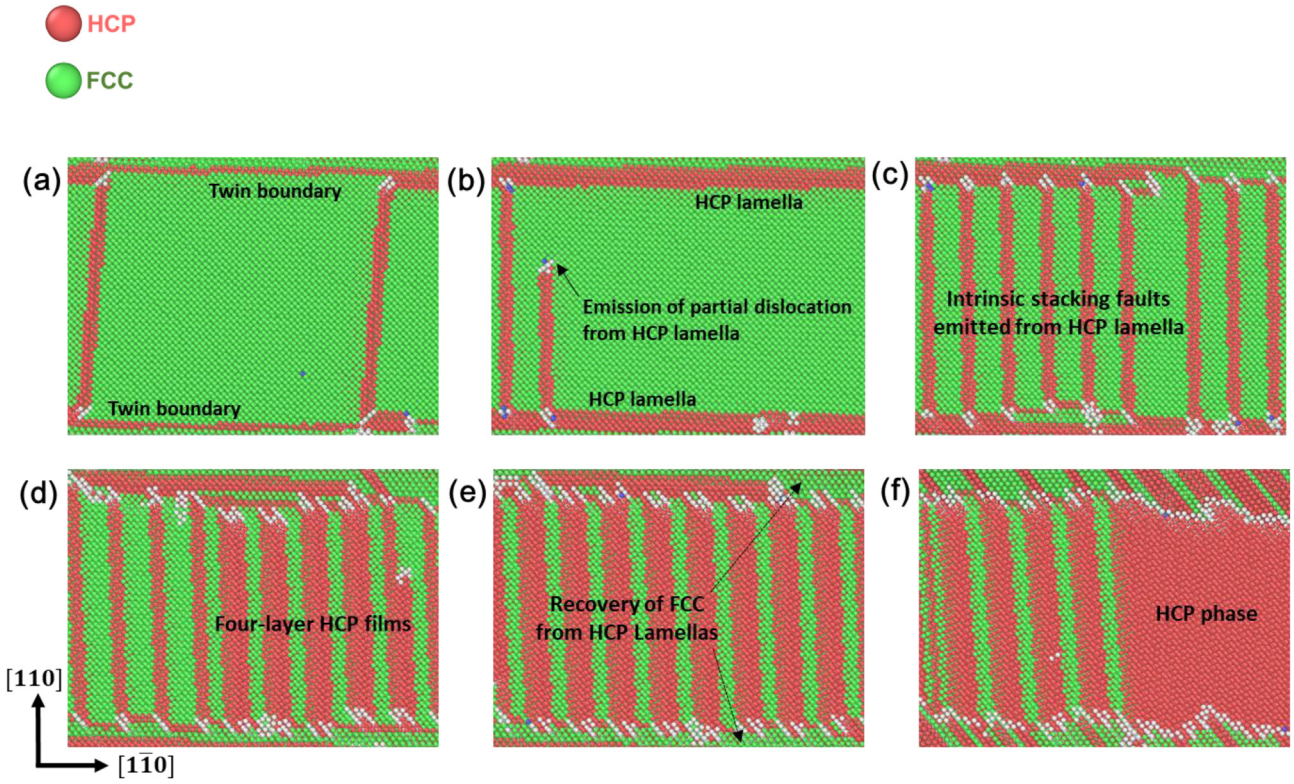

Fig. 4. Heterogeneous nucleation of Shockley partial dislocations at the fcc/hcp-lamella interfaces under sufficiently high compressive strain. In (a)-(d), the intrinsic stacking faults emitted from the fcc/hcp-lamella interface (or the twin boundary) may gradually transform into the four-layer hcp films via the successive glide of the new Shockley partials on their neighboring (1 1 1) atomic planes, which were eventually transformed into a bulk hcp region in (f). The green and brown colors indicate the fcc and hcp atoms, respectively, while the white colored atoms are the dislocation cores or the highly distorted atoms. (For interpretation of the references to colour in this figure legend, the reader is referred to the web version of this article.)

during the early stage of deformation turned out to be the most predominant mechanisms that facilitated the fcc-to-hcp phase transformation processes in the CoCrFeMnNi HEA under the [0 0 1] uniaxial compression. Our simulation results are basically in accord with some early experimental arguments on the fcc-to-hcp phase transformation mechanism in the Co-Fe alloy [55–57]. Mahajan et al.'s experiments evidenced the growth of the strain-induced hcp region from a non-coherent twin boundary of an annealing twin in the Co-6.25 wt% Fe alloy. They proposed that the hcp martensite could be arising from the propagation of one out of every two Shockley partials residing on a twin boundary to form the four- or six-layer hcp nuclei, thereby further growing into a macroscopically observable hcp region in the fcc lattice [55,56]. Furthermore, Singh et al. also claimed that the non-coherent twin boundaries can play a critical role in providing Shockley partial dislocations to assist in driving the thermally induced fcc-to-hcp phase transformation in the Co-5 wt% Fe alloy while the influences of grain boundaries and crystal surfaces appeared to be rather insignificant [57]. Since the fcc Co-5 wt% Fe alloy is also a material system with the negative stacking fault energy in nature, the strain-induced fcc-to-hcp phase transformation behaviors in this alloy system are expected to be very similar to those found in the CoCrFeMnNi HEA.

3.2. Uniaxial compressions along the [1 1 0] and [11$\bar{1}$] direction

As for the uniaxial compressions on the fcc CoCrFeMnNi HEA along the [1 1 0] and [1$\bar{1}$1] directions, we have observed somewhat different strain-relaxation mechanisms in our MD simulations during the plastic deformation processes. Although the structural relaxation still proceeded primarily with the nucleation and glide of Shockley partial dislocation loops, it did not lead to the significant fcc-to-hcp phase transformation in the CoCrFeMnNi HEA when the applied compressive loadings were along these two directions, respectively. Figs. 5 and 6 present the structural evolutions of the fcc CoCrFeMnNi HEA under compressive loadings at various stages of strain levels along the [1 1 0] and [1$\bar{1}$1] directions, respectively. As the strain level was raised above 30.0%, both of these two systems have nearly reached an equilibrium state and ended up with 19.2% and 10.3% of the constituent elements transformed into the hcp atoms, respectively, which were remarkably lower than that in the system upon the [0 0 1] uniaxial compression. Furthermore, it can be noticed that there were almost no apparent bulk hcp regions formed in the fcc matrix while most of the hcp atoms either constituted the nanoscale domains or simply formed the intrinsic stacking faults as the CoCrFeMnNi HEA was subjected to the [1 1 0] and [1$\bar{1}$1] uniaxial compressions. Our MD simulations also revealed that there were almost no large extended stacking faults, hcp-lamellas, and deformation-twinned regions created during the plastic deformation processes in these two uniaxially-compressed HEA systems. Accordingly, these simulation results also infer that the twin boundaries, hcp lamellas, and large extended stacking faults created during the early stages of deformation can indeed play a critical role in facilitating the fcc-to-hcp phase transformation in the CoCrFeMnNi HEA under a high compressive-loading environment.

Fig. 7(a) and (b) display the simulated stress-strain and resolved shear stress-strain curves for the fcc CoCrFeMnNi HEA under uniaxial compressions along the [0 0 1], [1 1 0], and [1$\bar{1}$1] directions, respectively. It was found that the homogeneous nucleation of dislocation loops first occurred as the strain level was increased up to 8.0 and 11.0% with a compressive stress (resolved shear stress) of ~34.5 (~16.2) and 36.0 (~11.0) GPa for the [1 1 0] and [1$\bar{1}$1] uniaxial compressions, respectively, which were considerably higher than the onset stress of plastic deformation for the [0 0 1] uniaxial compression (9.5 GPa). The much higher critical resolved shear stress of plastic deformation for the [1 1 0] and [1$\bar{1}$1] uniaxial compressions can be primarily attributed to the relatively large Young's moduli along these two directions (E_{110} = 265 GPa vs. E_{111} = 296 GPa), which are about twofold greater than that along the [0 0 1] direction (E_{001} = 144 GPa). In addition, the orientation dependence of the critical resolved shear stress (yield stress) can be also due to the different relaxation modes that may proceed as the CoCrFeMnNi HEA was subjected to different uniaxial compressions. Such an orientation dependence of the critical resolved shear stress (yield stress) have also been evidenced in other single-crystal metallic systems, such as fcc Cu [58] and $L1_2$ Ni_3(Ge, Al, Nb) alloys [59,60], etc. Very recently, Okamoto et al. reported that there was no clear orientation dependence of the critical resolved shear stress (CRSS) for the {1 1 1} ⟨1 1 0⟩ slip in the CoCrFeMnNi HEA [61]. In their experiment, however, only two different orientations of the loading axes, [$\bar{1}$23] and [$\bar{1}$26], were employed for their compression tests. It is worth noting that the angle between these two high-index orientations, [$\bar{1}$23] and [$\bar{1}$26], is simply 16°, while the angles between the [0 0 1] and [1 1 1], [0 0 1] and [1 1 0], and [1 1 1] and [1 1 0] orientations are 55°, 45°, and 35°, respectively. It can be expected that the difference of the observed CRSS between the two loading axes with a small angle variation can be relatively small. Accordingly, the orientation dependence of the CRSS in the CoCrFeMnNi HEA is possible to become much clearer as the angle between the two compressive loading axes is raised up to a certain level.

Fig. 7(c) displays the calculated dislocation densities for the fcc CoCrFeMnNi HEA under uniaxial compressions along the [0 0 1], [1 1 0], and [1$\bar{1}$1] directions, respectively. Herein the dislocation densities, including both Shockley partials and Lomer-Cottrell dislocations, were calculated using the open software, Ovito, which performs the dislocation analysis based on Stukowski et al.'s method [62]. It can be noticed that the dislocation density of the system upon the [0 0 1] uniaxial compression was substantially lower than that of the other two systems during the early stage of deformation, but then it rapidly increased and became comparable with the other two systems as the strain level was raised up to ~27%. The rapid increase of the dislocation density as the strain level was raised above 15% in the [0 0 1] uniaxial compression system was mainly attributed to that fact that there were numerous dislocations reactions occurred near the twin boundaries and the fcc/hcp-lamella interfaces. For the system under the [1$\bar{1}$1] uniaxial compression, however, the dislocation density was relatively high at the early beginning, but then it gradually decreased to a steady value as the strain level was increased up more than 20%. Very interestingly, as for the [1 1 0] uniaxial compression, the dislocation density appeared to be nearly unchanged during the whole deformation process. These calculations clearly indicate that the uniaxial compression system with a much higher onset stress of plastic deformation may lead to a higher dislocation density during the early stage of deformation. Furthermore, our simulation results also reveal an important fact that the phase transformation and strain relaxation behaviors in the CoCrFeMnNi HEA under high compressive loading are strongly crystal orientation-dependent. Although the [0 0 1] uniaxial compression produced a much lower dislocation density in the CoCrFeMnNi HEA than the other two uniaxial compression systems, it turned out to induce a much higher percentage of the constituent elements transformed into the hcp atoms during the whole plastic deformation process.

Fig. 8 presents the calculated densities of Shockley partial and Lomer-Cottrell dislocations for the fcc CoCrFeMnNi HEA under uniaxial compressions along the [0 0 1], [1 1 0], and [1$\bar{1}$1] directions, respectively. It can be found that the Shockley partial dislocation densities of the [1 1 0] and [1$\bar{1}$1] uniaxial compression systems were more than three times greater than that under the [0 0 1] uniaxial compression during the early stage of deformation (i.e., strain levels < 20%). As a consequence, there would be much more dislocation-dislocation interactions between Shockley partials gliding on different {1 1 1} planes in these two systems, which can therefore have higher chances to result in the annihilation of dislocations or move further to form the sessile stair-rod dislocation junctions such as the Lomer-Cottrell and Hirth lock dislocations than the [0 0 1] uniaxial compression system. These immobile dislocation junctions can act as the barriers to hinder the movement of Shockley partial dislocations, thereby causing the

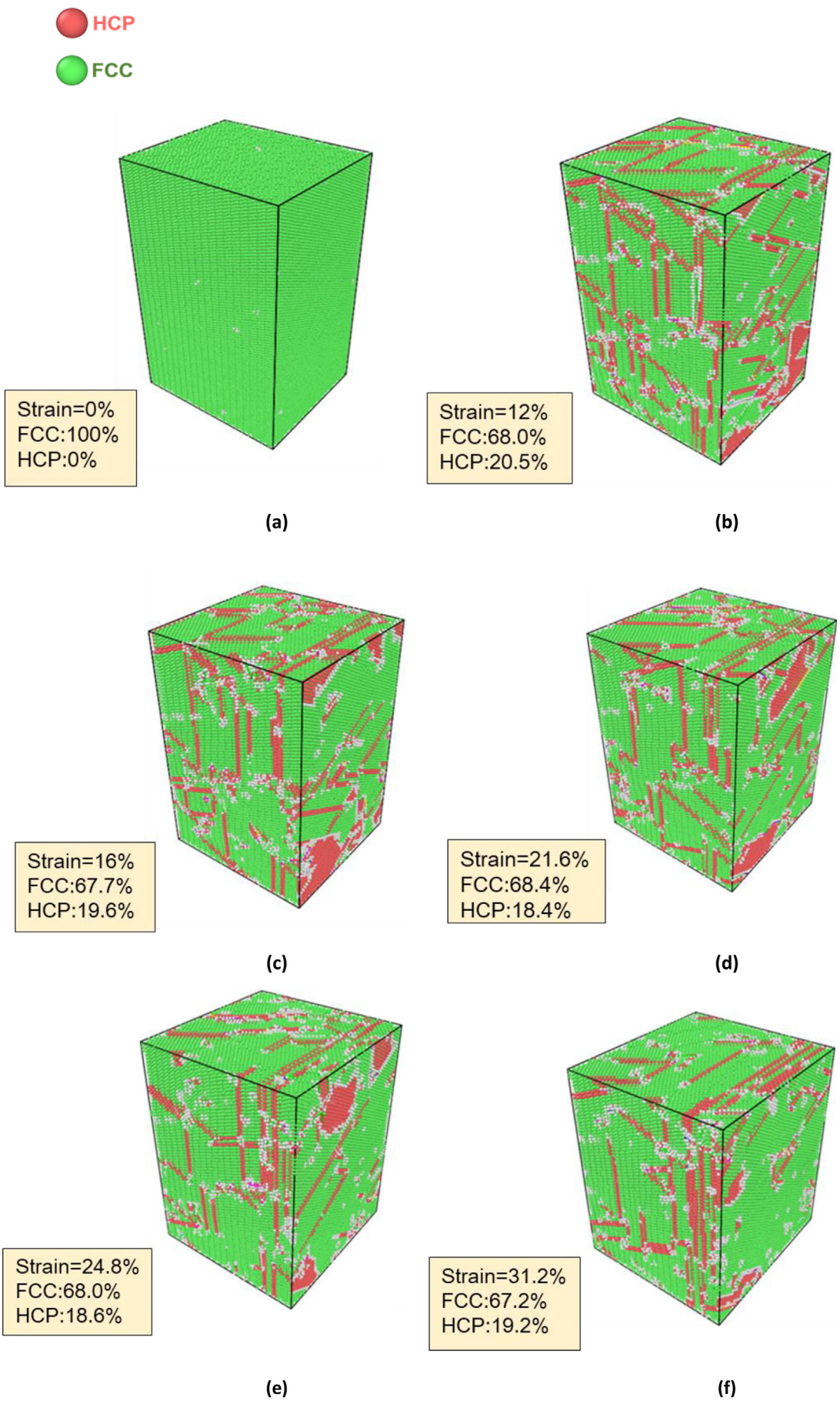

(caption on next page)

Fig. 5. The structural evolution of the fcc CoCrFeMnNi HEA upon compressive loading along the [1 1 0] direction at various stages of strain levels. The green and brown colors indicate the atoms in the perfect fcc and hcp lattice arrangements, respectively, while the white colored atoms represent the dislocation cores or the highly distorted atoms. (For interpretation of the references to colour in this figure legend, the reader is referred to the web version of this article.)

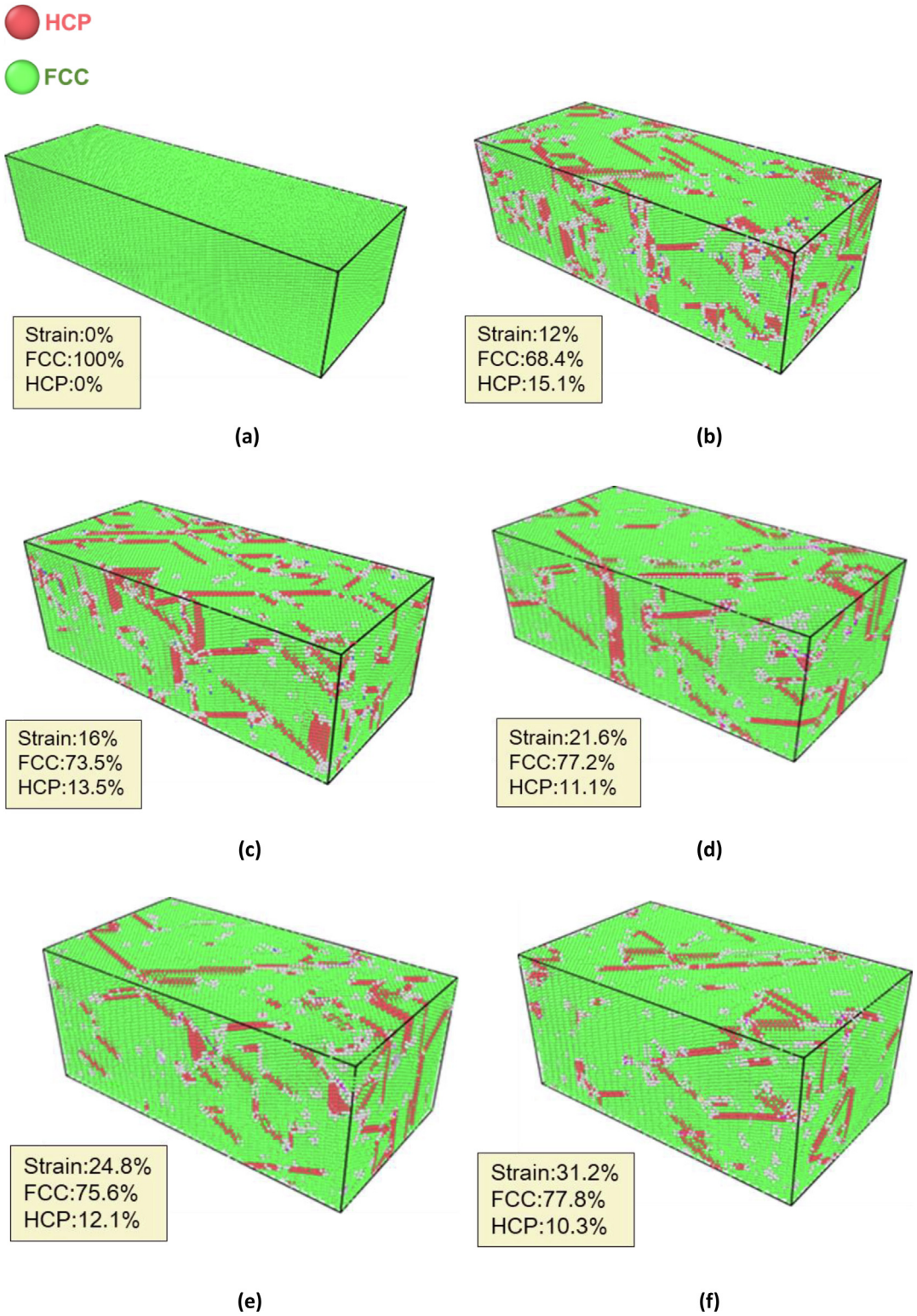

Fig. 6. The structural evolution of the fcc CoCrFeMnNi HEA upon compressive loading along the $[1\bar{1}1]$ direction at various stages of strain levels. The green and brown colors indicate the atoms in the perfect fcc and hcp lattice arrangements, respectively, while the white colored atoms represent the dislocation cores or the highly distorted atoms. (For interpretation of the references to colour in this figure legend, the reader is referred to the web version of this article.)

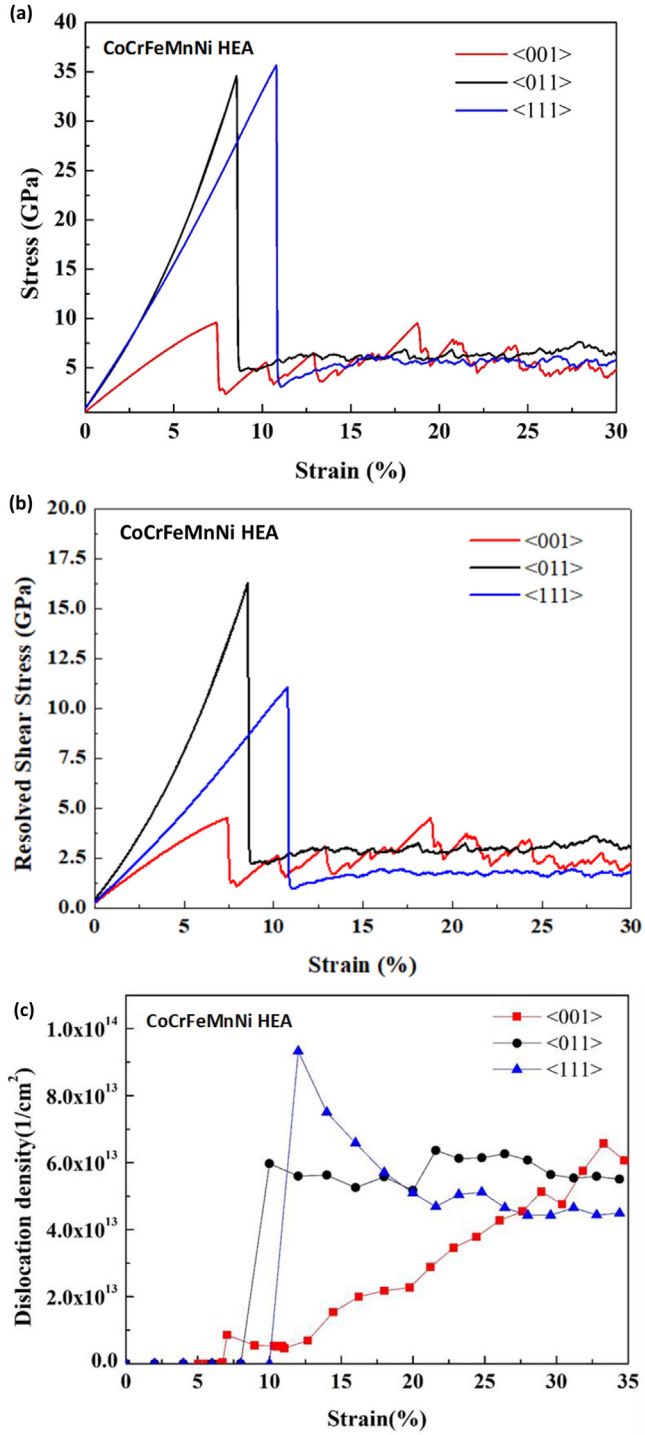

Fig. 7. The calculated (a) stress–strain curves, (b) resolved shear stress–strain curves, and (c) dislocation densities for the fcc CoCrFeMnNi HEA under uniaxial compressions along the [0 0 1], [1 1 0] and [1$\bar{1}$1] directions, respectively. The resolved shear stresses for the [0 0 1] and [1 1 0] uniaxial compressions were calculated for the most favorable (1 1 1)[11$\bar{2}$] partial slip system; for the [1$\bar{1}$1] uniaxial compression, the resolved shear stresses were calculated for the (1 1 1) [$\bar{1}$21] partial slip system.

substantial reduction of their glide mobility and the associated plastic deformation behaviors in the [1 1 0] and [1$\bar{1}$1] uniaxial compression systems. These calculated results can thus appropriately account for the reason why there were no large extended stacking faults, extended hcp-lamellas, and large deformation twinned regions created during the plastic deformation processes in these two uniaxial compression systems. Accordingly, there were no significant fcc-to-hcp phase transformation occurred as well as no obvious bulk hcp phase formed in the fcc matrix as the CoCrFeMnNi HEA were subjected to the [1 1 0] and [1$\bar{1}$1] uniaxial compressions, respectively. On the other hand, we have also calculated the energy differences between hcp and fcc phases as the CoCrFeMnNi HEA were subjected to the [0 0 1], [1 1 0], and [1$\bar{1}$1] uniaxial compressions, respectively, from 0 to 8% without the formation of any dislocation. The calculated results were displayed in the supplementary Fig. S3, which revealed that the stability of the fcc phase was substantially increased as compared with the hcp structure upon the [0 0 1] uniaxial compression; however, the stability of the hcp phase was found to be further enhanced in comparison to the fcc structure upon the [1 1 0] and [1$\bar{1}$1] uniaxial compressions, respectively. These results are in accord well with the calculated dislocation densities shown in Fig. 8, where the [1 1 0] and [1$\bar{1}$1] uniaxial compression systems both have a relatively higher partial dislocation density than the [0 0 1] system, but appear to have no direct influence on the phase transformation behaviors observed in the MD simulations. Therefore, the energy differences between hcp and fcc phases as the CoCrFeMnNi HEA was subjected to a particular strain condition may not play a decisive role in driving the fcc-to-hcp phase transformation in the highly compressed CoCrFeMnNi HEA. Furthermore, since the onset stress of plastic deformation is relatively high for the [1 1 0] and [1$\bar{1}$1] uniaxial compressions, the experimentally observed fcc-to-hcp phase transformation in the hydrostatically-compressed CoCrFeMnNi HEA can be predominantly attributed to the induced compressive strain along the [0 0 1] direction.

3.3. Constrained uniaxial compression along the [0 0 1] direction

To understand the non-hydrostatic effect on the pressure-induced phase transformation behavior in the CoCrFeMnNi HEA, we have carried out MD simulations to investigate the system upon the [0 0 1] uniaxial compression with the other two unstrained boundaries (i.e., [1 0 0] and [0 1 0]) being fixed during the whole plastic deformation process. Fig. 9 presents the snapshots of the structural evolution of the fcc CoCrFeMnNi HEA upon the constrained [0 0 1] uniaxial compression at various stages of strain levels. Our results revealed that the fundamental mechanisms of plastic deformation and strain relaxation behaviors in this compressed CoCrFeMnNi HEA were nearly identical to those observed in the simulation system without any constraint on the lateral boundaries along the unstrained directions. The structural relaxation mechanism during the early stage of deformation still proceeded primarily with the nucleation and glide of Shockley partial dislocation loops, followed by the formation of the intrinsic/extrinsic stacking faults and the deformation twined regions in the fcc lattice. However, the homogeneous nucleation of dislocation loops did not occur until the strain level was increased up to 12.0% with a relatively large imposed compressive stress of ~50.0 GPa along the [0 0 1] orientation (i.e. the critical resolved shear stress on the {1 1 1} planes by the [0 0 1] compressive strain was ~23.5 GPa), which was remarkably greater than that in the case without any constraint upon the [0 0 1] uniaxial compression.

Fig. 10 displays the calculated dislocation density and the resolved shear stresses on the {1 1 1} planes by the compressive stresses along the [0 0 1], [1 0 0], and [0 1 0] directions, respectively, for this constrained uniaxial compression system. It can be noted that the internal stresses increase more rapidly with the imposed compressive strain while the dislocation density is relatively lower than that in the system under the unconstrained [0 0 1] uniaxial compression. This was primarily because the effective resolved shear stress was largely reduced due to the induced compressive stresses by the two constrained boundaries along the [1 0 0] and [0 1 0] directions. Furthermore, although the interactions of Shockley partial dislocations with the extended stacking faults and twin boundaries can also lead to the

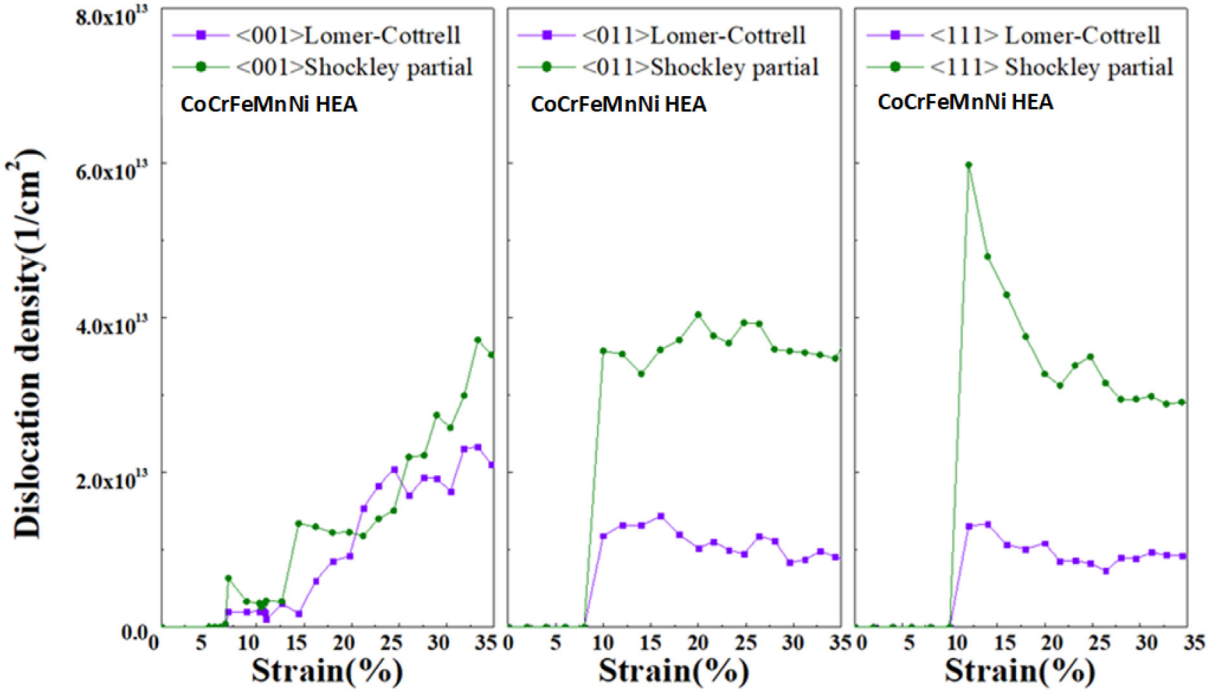

Fig. 8. The calculated densities of Shockley partial and Lomer-Cottrell dislocations for the fcc CoCrFeMnNi HEA under uniaxial compressions at various stages of strain levels along the [0 0 1], [1 1 0] and [1$\bar{1}$1] directions, respectively.

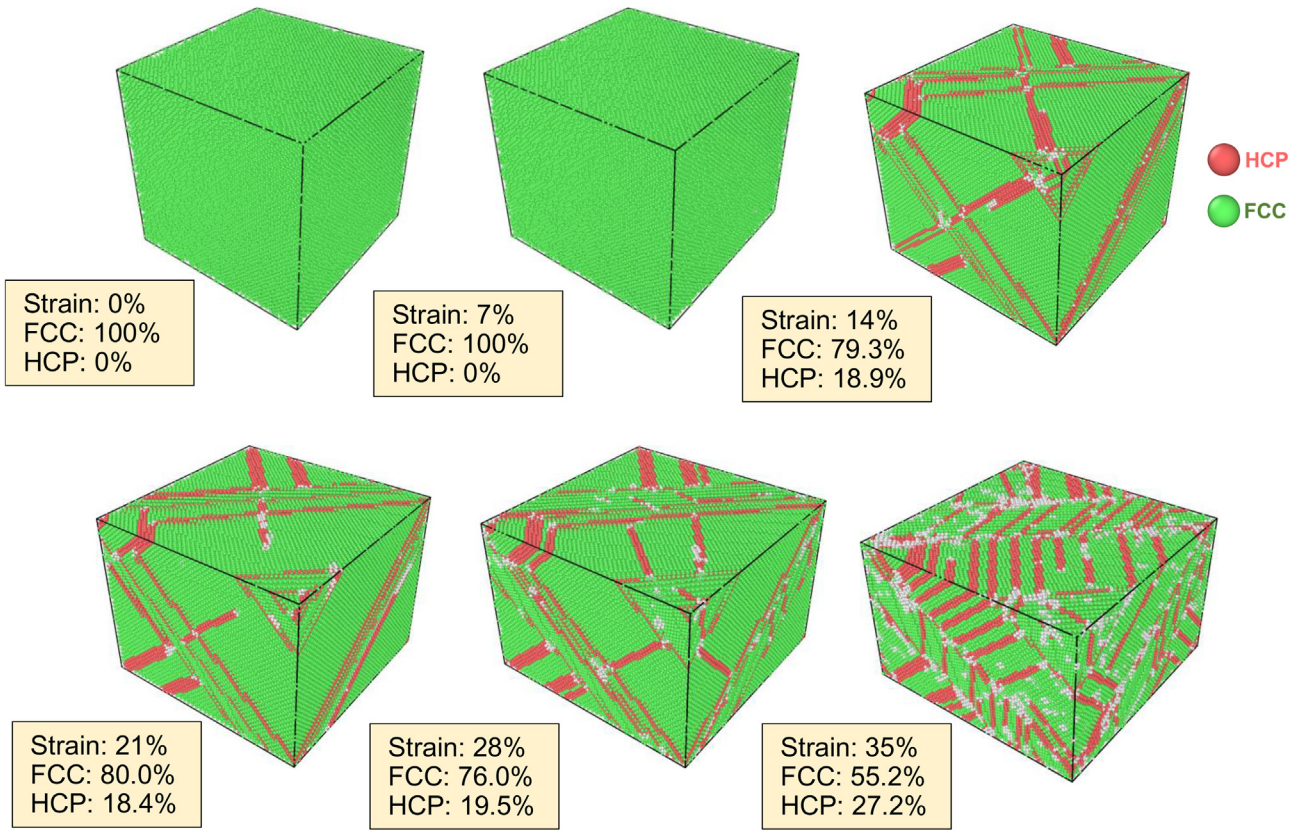

Fig. 9. The structural evolution of the fcc CoCrFeMnNi HEA upon the constrained [0 0 1] uniaxial compression at various stages of strain levels. The green and brown colors indicate the atoms in the perfect fcc and hcp lattice arrangements, respectively, while the white colored atoms represent the dislocation cores or the highly distorted atoms. (For interpretation of the references to colour in this figure legend, the reader is referred to the web version of this article.)

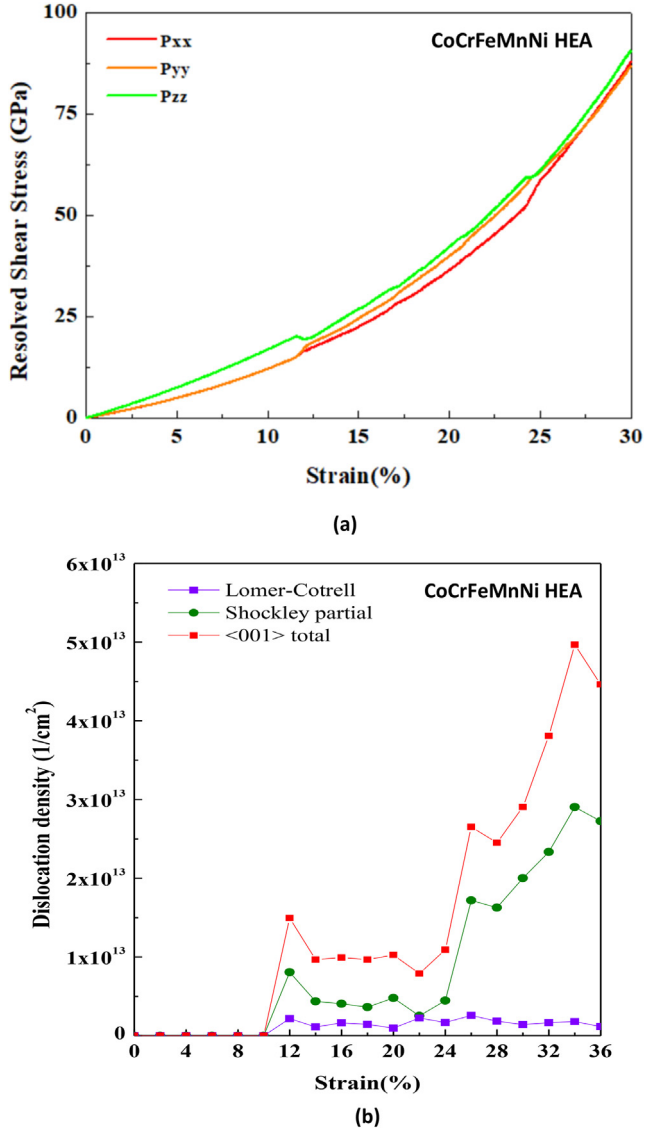

Fig. 10. The calculated (a) resolved shear stress-strain curves and (b) the dislocation densities for the fcc CoCrFeMnNi HEA under the constrained [0 0 1] uniaxial compression with the other two unstrained boundaries along the [1 0 0] and [0 1 0] directions being fixed upon deformation. The resolved shear stresses for the [0 0 1] uniaxial compression were calculated for the most favorable (1 1 1)[11$\bar{2}$] partial slip system, while those for the induced compressive stresses along the [1 0 0] and [0 1 0] directions were calculated for the (1 1 1) [$\bar{2}$11] and (1 1 1)[1$\bar{2}$1] partial slip systems, respectively.

formation of hcp lamellas during the deformation process, nucleation and emissions of partial dislocations from these phase boundaries appeared to be significantly retarded due to the imposed boundary constraints along the unstrained directions. Accordingly, as the strain level was raised up to 35.0%, there were only 27.2% of the constituent elements transformed into the hcp atoms without the appearance of any bulk hcp region formed in the fcc matrix upon the end of phase transformation. These simulation results clearly indicated that the pressure-induced plastic deformation and fcc-to-hcp phase transformation processes in the CoCrFeMnNi HEA can be greatly enhanced by a locally anisotropic (non-hydrostatic) compression/constraint imposed; that is, the plastic deformation and phase transformation processes in the CoCrFeMnNi HEA can be effectively facilitated by a large deviatoric compressive stress while they may tend to be significantly retarded by imposing a hydrostatic compression. These calculated results are in excellent agreement with Zhang et al.'s recent *in situ* high-pressure XRD experiments [28]. Their results suggested that a large deviatoric compressive stress, τ [i. e. $\tau = \sigma_3 - \bar{\sigma}$; themeanstress$\bar{\sigma} = (\sigma_1 + \sigma_2 + \sigma_3)/3$, σ_1, σ_2, σ_3 are three principal stresses], induced by the non-hydrostaticity of the pressure medium can effectively reduce the onset pressure of phase transition, thereby facilitating the fcc-to-hcp phase transformation process in the fcc CoCrFeMnNi HEA. Therefore, our simulation results can provide a theoretical support for their experimental arguments and also help to elucidate the underlying mechanism of the non-hydrostatic effect on the phase transformation behavior in the fcc CoCrFeMnNi HEA.

3.4. Uniaxial compression on Ni

To compare the plastic deformation behaviors of the CoCrFeMnNi HEA with other fcc metals, we also carried out MD simulations to investigate the structural relaxation behaviors of pure nickel under uniaxial compressions along the [0 0 1], [0 1 1], and [1$\bar{1}$1] directions, respectively. The supplementary Fig. S4 presents the structural evolutions of Ni upon compressive loading along the [0 0 1] direction at various stages of strain levels. It can be found that the structural relaxation behavior in Ni upon the [0 0 1] uniaxial compression was very similar to that occurred in the fcc CoCrFeMnNi HEA during the early stage of deformation. The structural relaxation in Ni still proceeded primarily with the nucleation and glide of Shockley partial dislocation loops, followed by the formation of the stacking faults and deformation twinned regions in the fcc lattice. As the strain level further increased, emissions of partial dislocations from the twin boundaries also occurred upon deformation, but the dislocation nucleation density on the twin boundaries appeared to be significantly diminished as compared with that in the CoCrFeMnNi HEA. Furthermore, the interactions of Shockley partial dislocations with an existing twin boundary in Ni were only found to lead to the growth of the nano-twin region without the formation of the hcp lamellas along the twin boundary during the whole deformation process. As a consequence, only 20.7% of the Ni elements were converted into the hcp atoms as the strain level was raised up to 30%, and all of the hcp atoms simply constituted the stacking faults and the twin boundaries without the formation of any bulk hcp phase in the fcc matrix.

As for the uniaxial compressions on Ni along the [1 1 0] and [1$\bar{1}$1] directions, similar results were found as those occurred in the CoCrFeMnNi HEA as illustrated in the supplementary Figs. S5 and S6. As the strain level was increased to 30%, these two systems only ended up with 0.7% and 1.4% of the Ni elements converted into the hcp atoms, respectively, which were much less than that in the system under the [0 0 1] uniaxial compression. Moreover, there were also no apparent bulk hcp phase and deformation twinned regions formed upon deformation, and nearly all the hcp atoms simply constituted the intrinsic stacking faults in the fcc matrix. The supplementary Fig. S7 presents the calculated stress-strain curves and dislocation densities for Ni under uniaxial compressions, which shows that Ni has very similar deformation behaviors to those found in the CoCrFeMnNi HEA except that the compressed Ni has a much lower dislocation density than the HEA. These simulation results clearly indicate the similarity of the plastic deformation behaviors between the CoCrFeMnNi HEA and other fcc metals like Ni under a high compressive-loading environment. However, the main discrepancy in the fcc-to-hcp phase transformation behaviors can be predominantly attributed to the relatively lower stacking fault energy of the CoCrFeMnNi HEA than other fcc metals.

4. Conclusion

We have performed molecular dynamics simulations in conjunction with the 2NN MEAM potential to investigate the plastic deformation and fcc-to-hcp phase transformation mechanisms in the CoCrFeMnNi HEA under uniaxial compressions along the [0 0 1], [1 1 0] and [1$\bar{1}$1] directions, respectively. Our MD simulations revealed that the

structural relaxation in the highly compressed CoCrFeMnNi HEA proceeded primarily with the nucleation and glide of Shockley partial dislocation loops while the stress-induced phase transformation behaviors appeared to be strongly crystal orientation-dependent. The [0 0 1] uniaxial compression was found to induce significant fcc-to-hcp phase transformation and bulk hcp phase formation in the CoCrFeMnNi HEA via successive emissions of Shockley partial dislocations from the extended stacking faults, twin boundaries and the fcc/hcp-lamella interfaces created during the early stage of deformation. As for the [1 1 0] and [1$\bar{1}$1] uniaxial compression systems, however, the transformed hcp atoms can only constitute the nanoscale domains or simply form the intrinsic stacking faults without the formation of the deformation twinned regions and extended hcp lamellas in the fcc matrix. Although the [0 0 1] uniaxial compression produced a much lower dislocation density in the CoCrFeMnNi HEA than the other two uniaxial compression systems, it induced a much higher percentage of the constituent elements transformed into the hcp atoms during the whole plastic deformation process. Our simulation results clearly indicated that the deformation twin boundaries and extended hcp lamellas created during the early stage of deformation can indeed play a critical role in providing Shockley partial dislocations to effectively facilitate the fcc-to-hcp phase transformation in the CoCrFeMnNi HEA under high compression. These new findings are in great accord with some early experimental speculations on the fcc-to-hcp phase transformation mechanism in the Co-Fe alloy system.

On the other hand, our results showed that the plastic deformation and phase transformation in the CoCrFeMnNi HEA can be effectively facilitated by a large deviatoric compressive stress while they may tend to be significantly retarded by imposing a hydrostatic compression, in excellent agreement with the recent *in situ* high-pressure XRD experiments. Furthermore, our simulation results also demonstrated that the plastic deformation behaviors in Ni under uniaxial compressions are very similar to those occurred in the CoCrFeMnNi HEA, among which the [0 0 1] uniaxial compression induced a much higher percentage of the constituent elements transformed into the hcp atoms than the other two uniaxial compression systems. Under the [0 0 1] uniaxial compression, emissions of partial dislocations from the twin boundaries also occurred in Ni upon deformation but the dislocation nucleation density on the twin boundaries appeared to be significantly diminished. In addition, there were no hcp lamellas created along the twin boundaries during the plastic deformation processes in Ni. As a consequence, nearly all the hcp atoms simply constitute the intrinsic/extrinsic stacking faults without the formation of any bulk hcp phase in Ni under high compression. The main discrepancy in the phase transformation behaviors between Ni and the CoCrFeMnNi HEA can be largely attributed to the much lower stacking fault energy of the CoCrFeMnNi HEA than other fcc metals.

CRediT authorship contribution statement

Kang-Tien Hsieh: Formal analysis, Investigation, Data curation, Validation. **You-Yi Lin:** Formal analysis, Investigation, Data curation, Software. **Chi-Hung Lu:** Formal analysis, Investigation, Data curation, Validation. **Jer-Ren Yang:** Funding acquisition, Review. **Peter K. Liaw:** Review. **Chin-Lung Kuo:** Conceptualization, Methodology, Formal analysis, Investigation, Writing - original draft, Writing - review & editing, Supervision.

Declaration of Competing Interest

The authors declare that they have no known competing financial interests or personal relationships that could have appeared to influence the work reported in this paper.

Acknowledgments

CLK and JRY greatly acknowledge the Ministry of Science and Technology (MOST 106-2218-E-002-025) in Taiwan for their financial support of this project. We would also like to thank the National Center for High-Performance Computing in Taiwan and the NTU Computer and Information Networking Center for use of their high-performance computing facilities. PKL very much appreciates the support of (1) the U.S. Army Research Office project (W911NF-13-1-0438 and W911NF-19-2-0049) with the program managers, Drs. M. P. Bakas, S. N. Mathaudhu, and D. M. Stepp and (2) the National Science Foundation (DMR-1611180 and 1809640) with the program directors, Drs G. Shiflet and D. Farkas.

Data availability

The raw/processed data required to reproduce these findings cannot be shared at this time as the data also form part of an ongoing study.

Appendix A. Supplementary data

Supplementary data to this article can be found online at https://doi.org/10.1016/j.commatsci.2020.109864.

References

[1] J.W. Yeh, S.K. Chen, S.J. Lin, J.Y. Gan, T.S. Chin, T.T. Shun, C.H. Tsau, S.Y. Chang, Nanostructured high-entropy alloys with multiple principal elements: novel alloy design concepts and outcomes, Adv. Eng. Mater. 6 (2004) 299–303.
[2] B. Gludovatz, A. Hohenwarter, D. Catoor, E.H. Chang, E.P. George, R.O. Ritchie, A fracture-resistant high-entropy alloy for cryogenic applications, Science 345 (2014) 1153–1158.
[3] B. Cantor, Multicomponent and high entropy alloys, Entropy 16 (2014) 4749–4768.
[4] D.B. Miracle, J.D. Miller, O.N. Senkov, C. Woodward, M.D. Uchic, J. Tiley, Exploration and development of high entropy alloys for structural applications, Entropy 16 (2014) 494–525.
[5] Y. Zhang, G.M. Stocks, K. Jin, C. Lu, H. Bei, B.C. Sales, L. Wang, L.K. Béland, R.E. Stoller, G.D. Samolyuk, M. Caro, A. Caro, W.J. Weber, Influence of chemical disorder on energy dissipation and defect evolution in concentrated solid solution alloys, Nat. Comm. 6 (2015) 8736.
[6] C. Lu, L. Niu, N. Chen, K. Jin, T. Yang, P. Xiu, Y. Zhang, F. Gao, H. Bei, S. Shi, M.-R. He, I.M. Robertson, W.J. Weber, L. Wang, Enhancing radiation tolerance by controlling defect mobility and migration pathways in multicomponent single-phase alloys, Nat. Commun. 7 (2016) 13564.
[7] F. Granberg, K. Nordlund, M.W. Ullah, K. Jin, C. Lu, H. Bei, L.M. Wang, F. Djurabekova, W.J. Weber, Y. Zhang, Mechanism of radiation damage reduction in equiatomic multicomponent single phase alloys, Phys. Rev. Lett. 116 (2016) 135504.
[8] Y. Zhang, S. Zhao, W.J. Weber, K. Nordlund, F. Granbergc, F. Djurabekova, Atomic-level heterogeneity and defect dynamics in concentrated solidsolution alloys, Curr. Opin. Solid State Mater. Sci. 21 (2017) 221–237.
[9] Y. Zhang, K. Jin, H. Xue, C. Lu, R.J. Olsen, L.K. Beland, M.W. Ullah, S. Zhao, H. Bei, D.S. Aidhy, G.D. Samolyuk, L. Wang, M. Caro, A. Caro, G.M. Stocks, B.C. Larson, I.M. Robertson, A.A. Correa, W.J. Weber, Influence of chemical disorder on energy dissipation and defect evolution in advanced alloys, J. Mater. Res. 31 (2016) 2363–2375.
[10] D.B. Miracle, O.N. Senkov, A critical review of high entropy alloys and related concepts, Acta Materialia 122 (2017) 448–511.
[11] L.J. Santodonato, Y. Zhang, M. Feygenson, C.M. Parish, M.C. Gao, R.J. Weber, J.C. Neuefeind, Z. Tang, P.K. Liaw, Deviation from high-entropy configurations in the atomic distributions of a multi-principal-element alloy, Nature Commun. 6 (2015) 5964.
[12] Y. Shi, B. Yang, P.K. Liaw, Corrosion-resistant high-entropy alloys: a review, Metals 7 (2017) 43.
[13] Z. Tang, T. Yuan, C. Tsai, J. Yeh, C.D. Lundin, P.K. Liaw, Fatigue behavior of a wrought Al0.5CoCrCuFeNi two-phase high-entropy alloy, Acta Mater. 99 (2015) 247–258.
[14] J.W. Yeh, Alloy design strategies and future trends in high-entropy alloys, JOM 65 (12) (2013) 1759–1771.
[15] Y. Zhang, T.T. Zuo, Z. Tang, M.C. Gao, K.A. Dahmen, P.K. Liaw, Z.P. Lu, Microstructures and properties of high-entropy alloys, Prog. Mater Sci. 61 (2014) 1–93.
[16] M.-H. Tsai, J.-W. Yeh, High-entropy alloys: a critical review, Mater. Res. Lett. 2 (2014) 107–123.
[17] F. Otto, A. Dlouhý, C. Somsen, H. Bei, G. Eggeler, E.P. George, The influences of temperature and microstructure on the tensile properties of a CoCrFeMnNi high-entropy alloy, Acta Mater. 61 (2013) 5743–5755.
[18] A. Gali, E.P. George, Tensile properties of high-and medium-entropy alloys,

Intermetallics 39 (2013) 74–78.
[19] D. Ma, B. Grabowski, F. Kormann, J. Neugebauer, D. Raabe, Ab initio thermodynamics of the CoCrFeMnNi high entropy alloy: importance of entropy contributions beyond the configurational one, Acta Mater. 100 (2015) 90–97.
[20] F. Tian, L.K. Varga, J. Shen, L. Vitos, Calculating elastic constants in high entropy alloys using the coherent potential approximation: current issues and errors, Comput. Mater. Sci. 111 (2016) 350–358.
[21] S. Zhao, G.M. Stocks, Y. Zhang, Stacking fault energies of face-centered cubic concentrated solid solution alloys, Acta Mater. 134 (2017) 334–345.
[22] C.L. Tracy, S. Park, D.R. Rittman, S.J. Zinkle, H. Bei, M. Lang, R.C. Ewing, W.L. Mao, High pressure synthesis of a hexagonal close-packed phase of the high-entropy alloy CrMnFeCoNi, Nat. Comm. 8 (2017) 15634.
[23] F. Zhang, Y. Wu, H. Lou, Z. Zeng, V.B. Prakapenka, E. Greenberg, Y. Ren, J. Yan, J.S. Okasinski, X. Liu, Y. Liu, Q. Zeng, Z. Lu, Polymorphism in a high-entropy alloy, Nat. Comm. 8 (2017) 15687.
[24] E.W. Huang, C.M. Lin, J. Jain, S.R. Shieh, C.P. Wang, Y.C. Chuang, Y.F. Liao, D.Z. Zhang, T. Huang, T.N. Lam, W. Woo, S.Y. Lee, Irreversible phase transformation in a CoCrFeMnNi high entropy alloy under hydrostatic compression, Mater. Today Commun. 14 (2018) 10–14.
[25] F.X. Zhang, S. Zhao, K. Jin, H. Bei, D. Popov, C. Park, J.C. Neuefeind, W.J. Weber, Y. Zhang, Pressure-induced fcc to hcp phase transition in Ni-based high entropy solid solution alloys, Appl. Phys. Lett. 110 (2017) 011902.
[26] A.S. Ahmad, Y. Su, S.Y. Liu, K. Ståhl, Y.D. Wu, X.D. Hui, U. Ruett, O. Gutowski, K. Glazyrin, H.P. Liermann, H. Franz, H. Wang, X.D. Wang, Q.P. Cao, D.X. Zhang, J.Z. Jiang, Structural stability of high entropy alloys under pressure and temperature, J. Appl. Phys. 121 (2017) 235901.
[27] P.F. Yu, L.J. Zhang, H. Cheng, H. Zhang, M.Z. Ma, Y.C. Li, G. Li, P.K. Liaw, R.P. Liu, The high-entropy alloys with high hardness and soft magnetic property prepared by mechanical alloying and high-pressure sintering, Intermetallics 70 (2016) 82–87.
[28] F. Zhang, H. Lou, S. Chen, X. Chen, Z. Zeng, J. Yan, W. Zhao, Y. Wu, Z. Lu, Q. Zeng, Effects of non-hydrostaticity and grain size on the pressure-induced phase transition of the CoCrFeMnNi high-entropy alloy, J. Appl. Phys. 124 (2018) 115901.
[29] M.I. Baskes, Modified embedded-atom method potentials for cubic materials and impurities, Phys. Rev. B 46 (1992) 2727–2742.
[30] B.J. Lee, M.I. Baskes, Second nearest-neighbor modified embedded-atom method potential, Phys. Rev. B 62 (2000) 8564–8567.
[31] B.J. Lee, J.H. Shim, M.I. Baskes, Semi-empirical atomic potentials for the FCC Metals Cu, Ag, Au, Ni, Pd, Pt, Al and Pb based on first and second nearest-neighbor modified embedded atom method, Phys. Rev. B 68 (2003) 144112.
[32] Y.M. Kim, B.J. Lee, M.I. Baskes, Modified embedded atom method interatomic potentials for Ti and Zr, Phys. Rev. B 74 (2006) 014101.
[33] Y.M. Kim, N.J. Kim, B.J. Lee, Atomistic modeling of pure Mg and Mg-Al system, CALPHAD 33 (2009) 650–657.
[34] W.M. Choi, Y.H. Jo, S.S. Sohn, S. Lee, B.J. Lee, Understanding the physical metallurgy of the CoCrFeMnNi high-entropy alloy: an atomistic simulation study, Comput. Mater. 4 (2018) 1.
[35] W.M. Choi, Y.M. Kim, D.H. Seol, B.J. Lee, Modified embedded-atom method interatomic potentials for the Co-Cr, Co-Fe, Co-Mn, Cr-Mn and Mn-Ni binary systems, Comput. Mater. Sci. 130 (2017) 121–129.
[36] Y.M. Kim, Y.H. Shin, B.J. Lee, Modified embedded-atom method interatomic potentials for pure Mn and Fe-Mn system, Acta Mater. 57 (2009) 474–485.
[37] W.P. Dong, H.K. Kim, W.S. Ko, B.M. Lee, B.J. Lee, Atomistic modeling of pure Co and Co-Al system, Calphad 38 (2012) 7–16.
[38] C. Wu, B.J. Lee, X. Su, Modified embedded-atom interatomic potential for Fe-Ni, Cr-Ni and Fe-Cr-Ni systems, CALPHAD 57 (2017) 98–106.
[39] Y.K. Kim, W.S. Jung, B.J. Lee, Modified embedded-atom method interatomic potentials for the Ni-Co binary and the Ni-Al-Co ternary systems, Model. Simul. Mater. Sci. Eng. 23 (2015) 055004.
[40] B.J. Lee, J.H. Shim, H.M. Park, A semi-empirical atomic potential for the Fe-Cr binary system, Calphad 25 (2001) 527–534.
[41] S. Plimpton, Fast parallel algorithms for short-range molecular dynamics, J. Comput. Phys. 117 (1995) 1–19.
[42] J.H. Rose, J.R. Smith, F. Guinea, J. Ferrante, Phys. Rev. B 29 (1984) 2963.
[43] G. Kresse, J. Hafner, Ab initio molecular dynamics for liquid metals, Phys. Rev. B 47 (1993) 558.
[44] G. Kresse, J.J. Furthmuller, Efficiency of ab-initio total energy calculations for metals and semiconductors using a plane-wave basis set, Comput. Mater., Sci. 6 (1996) 15–50.
[45] G. Kresse, J.J. Furthmuller, Efficient iterative schemes for ab initio total-energy calculations using a plane-wave basis set, Phys. Rev. B 54 (1996) 11169.
[46] J.M. Cowley, Short-range order and long-range order parameters, Phys. Rev. 138 (1965) A1384.
[47] J.M. Cowley, An approximate theory of order in alloys, Phys. Rev. 77 (1950) 669.
[48] J.D. Honeycutt, H.C. Anderson, J. Phys. Chem. 91 (1987) 4950.
[49] A. Stukowski, V.V. Bulatov, A. Arsenlis, Model. Simul. Mater. Sci. Eng. 25 (2012) 085007.
[50] C. Niu, C.R. LaRosa, J. Miao, M.J. Mills, M. Ghazisaeidi, Magnetically-driven phase transformation strengthening in high entropy alloys, Nat. Comm. 9 (2018) 1363.
[51] E.W. Huang, D. Yu, J.W. Yeh, C. Lee, K. An, S.Y. Tu, A study of lattice elasticity from low entropy metals to medium and high entropy alloys, Scripta Materialia 101 (2015) 32–35.
[52] M. Chassagne, M. Legros, D. Rodney, Atomic-scale simulation of screw dislocation/coherent twin boundary interaction in Al, Au, Cu and Ni, Acta Mater. 59 (2011) 1456–1463.
[53] Z.H. Jin, P. Gumbsch, E. Ma, K. Albe, K. Lu, H. Hahn, H. Gleiter, The interaction mechanism of screw dislocations with coherent twin boundaries in different face-centered cubic metals, Scr. Mater. 54 (2006) 1163–1168.
[54] M.D. Sangid, T. Ezaz, H. Sehitoglu, I.M. Robertson, Energy of slip transmission and nucleation at grain boundaries, Acta Mater. 59 (2011) 283–296.
[55] S. Mahajan, M.L. Green, D. Brasen, A model for the FCC→HCP transformation: its applications and experimental evidence, Metall. Trans. A 8A (1977) 283–293.
[56] S. Mahajan, D. Brasen, T. Wakiyama, Transformation-induced microstructures in cobalt-iron alloys, Metall. Trans. A 9A (1978) 1817–1824.
[57] J. Singh, S. Ranganathan, On the mechanism of FCC→HCP transformation, Phys. Stat. Sol. (a) 73 (1981) 243–248.
[58] X. Huang, A. Borrego, W. Pantleon, Polycrystal deformation and single crystal deformation: dislocation structure and flow stress in copper, Mater. Sci. Eng. A 319–321 (2001) 237–241.
[59] V.A. Starenchenko, E.V. Kozlov, YuV. Soloveva, YuA. Abzaev, N.A. Koneva, Orientation dependence of the yield stress and work-hardening rate of Ni3Ge at different temperatures, Mater. Sci. Eng. A 483–484 (2008) 602–606.
[60] C. Lall, S. Chin, D.P. Pope, The Orientation and temperature dependence of the yield stress of Ni_3(Al, Nb) single crystals, Metall. Trans. A 10 (1979) 1323–1332.
[61] N.L. Okamoto, S. Fujimoto, Y. Kambara, M. Kawamura, Z.M.T. Chen, H. Matsunoshita, K. Tanaka, H. Inui, E.P. George, Size effect, critical resolved shear stress, stacking fault energy, and solid solution strengthening in the CrMnFeCoNi high-entropy alloy, Sci. Rep. 6 (2016) 35863.
[62] A. Stukowski, V.V. Bulatov, A. Arsenlis, Automated identification and indexing of dislocations in crystal interfaces, Modelling Simul. Mater. Sci. Eng. 20 (2012) 085007.